PAPER

Active manipulation of Helmholtz scalar fields: near-field synthesis with directional far-field control

View the article online for updates and enhancements.

Active manipulation of Helmholtz scalar fields: near-field synthesis with directional far-field control

Neil Jerome A Egarguin[1,2,4] ⓘ**, Daniel Onofrei**[1]**,**
Chaoxian Qi[3] **and Jiefu Chen**[3]

[1] Department of Mathematics, University of Houston, Houston, TX, United States of America
[2] Institute of Mathematical Sciences and Physics, University of the Philippines Los Baños College, Laguna, The Philippines
[3] Department of Electrical and Computer Engineering, University of Houston, Houston, TX, United States of America

E-mail: naegarguin1@up.edu.ph

CrossMark

Abstract

In this article, we propose a strategy for the active manipulation of scalar Helmholtz fields in bounded near-field regions of an active source while maintaining desired radiation patterns in prescribed far-field directions. This control problem is considered in two environments: free space and homogeneous ocean of constant depth, respectively. In both media, we proved the existence of and characterized the surface input, modeled as Neumann data (normal velocity) or Dirichlet data (surface pressure) such that the radiated field satisfies the control constraints. We also provide a numerical strategy to construct this predicted surface input by using a method of moments-approach with a Morozov discrepancy principle-based Tikhonov regularization. Several numerical simulations are presented to demonstrate the proposed scheme in scenarios relevant to practical applications.

Keywords: active acoustic control, scalar Helmholtz fields, acoustics in homogeneous ocean, directional far-field radiation control, Tikhonov regularization

(Some figures may appear in colour only in the online journal)

[4] Author to whom any correspondence should be addressed.

1. Introduction

The active control of acoustic fields in various media has been a very active area of research due to the multitude of possible practical applications. These include the creation of personal audio systems or multizone sound synthesis and reproduction ([34, 38, 47, 50] and references therein), acoustic imaging ([15, 16, 29] and references therein), active noise control ([5, 23, 24, 26, 36] and references therein) and acoustic shielding and cloaking ([4, 13, 14, 20, 35, 39] and references therein). In particular, the manipulation of Helmholtz fields in underwater environments is widely-studied as it presents important applications such as in communications, ocean imaging and remote sensing, marine ecosystem monitoring [52] and military and defense applications [28] (see also the monograph [22] for a detailed discussion of computational strategies for ocean acoustics). In [6, 46], comprehensive discussions of the development of underwater acoustic networks and the challenges involved were provided. The complexity of the make-up of the ocean environment requires substantial modification of control strategies designed for free space (or other simple media). As such, existing free space strategies are adapted to simpler marine environments like shallow water or a homogeneous finite-depth ocean (see for example the reference monographs [2, 22]). For instance, in [32], the authors proposed the use of acoustic contrast control strategies to focus sound in shallow water. In the same environment, the works [3, 43] developed a single-mode excitation with a feedback control algorithm to achieve both near- and far-field sound control.

The manipulation of the acoustic far field poses several challenges, such as loss of evanescent fields and diffraction limits. In [33], the authors broached a method to overcome these limits and attained effective far-field imaging using wave vector filtering. In [31] far-field time reversal was used to overcome those challenges. Another approach is the smart design of transducers with adaptive structures such as classical rectangular panels in an infinite baffle [42], foldable tessellated star transducers [53], Helmholtz resonators with computerized controls [30] and modern metamaterials [49].

From the numerical point of view, finite-element methods (FEM) have been continually refined to address some of the shortcomings of the classical FEM, such as those encountered involving acoustic scattering in unbounded domains, numerical dispersion errors and heavy computational requirements especially for adaptive methods. Some recent advances on this front can be found in [19, 48]. Several numerical methods employing optimization frameworks are also used especially in solving acoustic inverse problems for biomedical imaging [45], subsurface imaging [7] and sound propagation in waveguides [27]. Other approaches include wave-domain methods (as used in [17, 18]) and modal-domain approaches (for instance [37, 51]). The approach employed in this paper (as well as previous works such as [11, 12, 21, 39, 40]) is the use of the Green's function to represent the solution to the Helmholtz equation in terms of a propagator operator and then employ a Tikhonov regulariation scheme with the Morozov discrepancy principle to solve the resulting operatorial equation. For underwater acoustic control problems, three strategies are commonly used in expressing the propagated field (see [22, 25] for a discussion of each approach), namely normal modes, the Hankel transform and the ray representation (or the multiple reflection representation for stratified oceans).

In our previous works [11, 39, 40], we used global basis representation of the desired inputs in the spirit of [10]. In this paper, we present new theoretical results and propose novel numerical schemes on the active control of acoustic fields in free space and in a homogeneous ocean of finite depth. These results enhance our previous works by allowing for additional constraints on the fields' radiated far-field pattern. Thus, in this work we are able to prove and numerically validate the possibility of characterizing active sources (represented as surface pressure

or normal velocities) so that the field generated will approximate given patterns in prescribed exterior regions while maintaining desired far-field radiation in fixed directions.

The main novelty of this paper is the simultaneous active control of near fields in prescribed exterior bounded regions and various far-field directions with different prescribed far-field patterns in two separate environments: free space and homogeneous finite-depth ocean environment. In [11, 39, 40], only near region field control and the case of an almost nonradiating source were considered. In the latter, a null field was prescribed in the entire far-field region which is a far stronger condition than the one considered in the current study where we allow different far-field radiation patterns to be prescribed in different fixed far-field directions. This additional constraint gave rise to a new functional framework and additional layers in the numerical scheme. Moreover, [40] only offered a brief discussion of the theoretical results for the active acoustic control in homogeneous finite-depth ocean environment and did not provide any numerical investigations. Last, but not least we propose here the use of local basis functions to represent the unknown boundary input instead of global basis functions (e.g., spherical harmonics) as used in the aforementioned works. This improved the computation time required for the simulations, especially since the additional far-field constraints significantly increased the problem's complexity. This choice may also aid in the physical instantiation of the calculated boundary input as fewer degrees of freedom are now needed to achieve good control accuracy.

The rest of the paper is organized as follows. Section 2 formally states the mathematical formulation of the general problem. Sections 3 and 4 present the analysis and numerical results in free space and homogeneous finite-depth ocean environments, respectively. Both of these sections includes subsections discussing the theoretical results and numerical simulations. We end with concluding statements and future research directions in section 5.

2. Statement of the problem

We consider the problem of characterizing an active source (modeled as surface pressure or surface normal velocity) to accurately approximate *a priori* given fields in several bounded exterior regions while synthesizing different desired patterns in various prescribed far-field directions. Let $D_a \Subset R$ (where R denotes the environment space to be defined below and $\Subset$ denotes a compact embedding) be the active source modeled as a compact region in space with Lipschitz continuous boundary and $\{R_1, R_2, \ldots, R_m\}$ be a collection of m mutually disjoint smooth domains exterior to D_a. Moreover, we consider n distinct directions $\hat{\mathbf{x}}_1, \hat{\mathbf{x}}_2, \ldots, \hat{\mathbf{x}}_n$ representing the far-field directions of interest. Mathematically, the problem is to find a boundary input on the source, either a Neumann input data $v \in C(\partial D_a)$ (normal velocity) or a Dirichlet data $p \in C(\partial D_a)$ (pressure) such that for any desired field $f = (f_1, f_2, \ldots, f_m)$ on the control regions (i.e., for each l, f_l solves the homogeneous Helmholtz equations in some neighborhood of R_l) and prescribed far-field pattern values $f_\infty = (f_{\infty,1}, f_{\infty,2}, \ldots, f_{\infty,n})$, the solution u of the following exterior Helmholtz problem:

$$
\begin{cases}
\Delta u + k^2 u = 0 \text{ in } R \backslash D_a, \\
\nabla u \cdot \mathbf{n} = v, (\text{or } u = p) \text{ on } \partial D_a \\
\text{boundary conditions corresponding to the medium} \\
\text{suitable radiation condition in the medium}
\end{cases}
\tag{1}
$$

and its corresponding far-field pattern u_∞ satisfies

$$\begin{cases} \|u - f_l\|_{C^2(R_l)} \leqslant \mu & \text{for } l = \overline{1, m} \\ |u_\infty(\hat{\mathbf{x}}_j) - f_{\infty, j}| \leqslant \mu & \text{for } j = \overline{1, n} \end{cases} \tag{2}$$

for a desired small positive accuracy threshold μ. Here and throughout the rest of the paper $\mathbf{n}$ is the outward unit normal to ∂D_a and $\hat{\mathbf{x}} = \frac{\mathbf{x}}{|\mathbf{x}|}$ denotes the unit vector along the direction $\mathbf{x}$. Moreover, the $\mathrm{e}^{-\mathrm{i}\omega t}$-dependence of the fields, where $\omega = kc$ and c is the propagation speed of sound in the respective media, is implicitly assumed and omitted. For the free space environment, $R = \mathbb{R}^3$, the radiation condition is

$$\langle \hat{\mathbf{x}}, \nabla u(\mathbf{x}) \rangle - \mathrm{i}ku(\mathbf{x}) = o\left(\frac{1}{|\mathbf{x}|}\right), \quad \text{as } |\mathbf{x}| \to \infty \text{ uniformly for all } \hat{\mathbf{x}} \tag{3}$$

and there are no additional boundary conditions. Meanwhile the underwater environment is modeled as an homogeneous ocean with constant depth $-h > 0$ (see [2]) and we have $R = \{\mathbf{x} = (x, y, z) \in \mathbb{R}^3 | z \in [h, 0]\}$ with medium boundary conditions

$$\begin{cases} u = 0 \text{ at the ocean surface } z = 0 \text{ and} \\ \dfrac{\partial u}{\partial z} = 0 \text{ at the ocean floor } z = h \end{cases}. \tag{4}$$

The radiation condition for this environment is given in section 4.1.

Classical results (for instance, [2, 9]) guarantee that for every set of given Dirichlet or Neumann inputs on ∂D_a, problem (1) has a unique continuous radiating solution u (with the additional condition that the normal derivative exists in the sense of uniform convergence for the Neumann problem). Building-up the strategy used in [11, 39, 40] we analyze a representation for the unique solution of the above exterior problem as a function of the inputs and use this to characterize the boundary data that will ensure (2). We consider a fictitious source $D_a' \Subset D_a$ and slightly larger mutually disjoint open regions $W_1, W_2, \ldots, W_m$ with $R_l \Subset W_l$. We assume that for each l, f_l solves the homogeneous Helmholtz equations in W_l and also assume that the larger regions and the source are well separated, i.e.,

$$\overline{W_l} \cap \overline{D_a} = \emptyset, \quad \text{for } l = \overline{1, m}. \tag{5}$$

Lastly, we let $Y = \prod\limits_{l=1}^{m} L^2(\partial W_l)$ be the L^2 space of m-tuples of functions on the W_l's with the inner product

$$\langle \varphi, \psi \rangle_Y = \sum_{l=1}^{m} \langle \varphi_l, \psi_l \rangle_{L^2(\partial W_l)} \tag{6}$$

for all $\varphi = (\varphi_1, \varphi_2, \ldots, \varphi_m)$ and $\psi = (\psi_1, \psi_2, \ldots, \psi_m) \in Y$.

In the next two sections, we shall present the theoretical formulation and proof of the existence with explicit characterization of a class of solutions to the above questions backed with numerical simulations showing the feasibility of such a control scheme, for both the free space and homogeneous finite-depth ocean environment.

3. Free space environment

In this section, we shall deal with the problem of controlling the near field in various bounded exterior regions of space while creating prescribed far-field patterns in several directions in

a free-space environment using a single active source. We begin with the establishment of a proof of the existence of a solution for the active control problem (1)–(3). Then we propose a strategy for its explicit characterization and building on the numerical scheme developed in [11, 12, 40] we produce simulations supporting the current theoretical results.

3.1. Theoretical framework

It was shown in [39, 40] that if k is not a resonance wavenumber (see [8, 39, 40]), the normal velocity v or pressure p on the surface ∂D_a of the active source needed to solve the control problem (1)–(3) can be characterized by a density $w \in L^2(\partial D_a')$ such that

$$v(\mathbf{y}) = \frac{-\mathrm{i}}{\rho ck} \frac{\partial}{\partial \mathbf{n}} \int_{\partial D_a'} w(\mathbf{x})\phi(\mathbf{x}, \mathbf{y})\mathrm{d}S_{\mathbf{x}} \text{ and} \tag{7}$$

$$p(\mathbf{y}) = \int_{\partial D_a'} w(\mathbf{x})\phi(\mathbf{x}, \mathbf{y})\mathrm{d}S_{\mathbf{x}}, \tag{8}$$

where ρ denotes the density of the surrounding environment, c denotes the speed of sound in the given media and $\phi(\mathbf{x}, \mathbf{y}) = \frac{\mathrm{e}^{\mathrm{i}k|\mathbf{x}-\mathbf{y}|}}{4\pi|\mathbf{x}-\mathbf{y}|}$ is the fundamental solution of the 3D Helmholtz equation. The motivations behind (7) and (8) are summarized in the following remarks.

Remark 3.1. The expressions in (7) and (8) provide an ansatz for solutions of (1), (3). This ansatz is then used in a control argument to find a density w on a fictitious source D_a' so that the control constraints in (2) are satisfied.

Remark 3.2. The use of the fictitious source in the ansatz in (7) and (8) simplifies the analysis and calculations as D_a' can be chosen to be a sphere compactly embedded in the physical source. Recall that the physical source can assume any compact shape as long as it is well-separated from the control regions and has a Lipschitz continuous boundary to ensure the well-posedness of the exterior Helmholtz problem.

Remark 3.3. The boundary input obtained from the ansatz in (7) and (8) will be smooth. From a theoretical standpoint, this is desirable when the present scalar control results are extended to a vector Helmholtz or a Maxwell system (see [41]). From an applied perspective, smooth boundary inputs are often more suitable for practical applications as they are easier to approximate.

Although the expressions in (7) and (8) make use of the single layer potential operator, it was noted in [40] (see also [11]) that these inputs can be written in terms of the double layer potential operator and hence, also in terms of linear combinations of the two. Consequently, the results to be presented can be adapted to the case when the propagator operators are expressed in terms of a linear combination of the single and double layer potentials.

With this density $w \in L^2(\partial D_a')$, the field u satisfying (1) can be characterized on each control region by the operator $\mathcal{K} : L^2(\partial D_a') \to Y$, with

$$\mathcal{K}w(\mathbf{y}_1, \mathbf{y}_2, \ldots, \mathbf{y}_m) = \left(\mathcal{K}_1 w(\mathbf{y}_1), \mathcal{K}_2 w(\mathbf{y}_2), \ldots, \mathcal{K}_m w(\mathbf{y}_m)\right) \tag{9}$$

where for each $l = \overline{1, m}$, $\mathbf{y}_l \in \partial W_l$ and

$$\mathcal{K}_l w(\mathbf{y}_l) = \int_{\partial D_a'} w(\mathbf{x})\phi(\mathbf{x}, \mathbf{y}_l)\mathrm{d}S_{\mathbf{x}}. \tag{10}$$

From [9], the solution u has the asymptotic (far-field) expression

$$u(\mathbf{x}_0) = \frac{e^{ik|\mathbf{x}_0|}}{|\mathbf{x}_0|}\left(u_\infty(\hat{\mathbf{x}}_0) + \mathcal{O}\left(\frac{1}{|\mathbf{x}_0|}\right)\right) \tag{11}$$

uniformly in the direction $\hat{\mathbf{x}}_0$ as $|\hat{\mathbf{x}}_0| \to \infty$ and where the function u_∞ given by

$$u_\infty(\hat{\mathbf{x}}_0) = \frac{1}{4\pi}\int_{\partial D'_a} w(\mathbf{y})e^{-ik\hat{\mathbf{x}}_0 \cdot \mathbf{y}}dS_{\mathbf{y}} \tag{12}$$

is called the **far-field pattern** of u.

Remark 3.4.　The restriction that each f_l satisfies the Helmholtz equation in some neighborhood of R_l and the fact that $R_l \Subset W_l$ for all $1 \leqslant l \leqslant m$ ensure, through uniqueness and regularity results for the interior Helmholtz problems (in the spirit of [39]), that the field u, solution of (1), (3), will satisfy the control constraint (2) if

$$\begin{cases} \|u - f_l\|_{L^2(\partial W_l)} \leqslant \mu & \text{for } l = \overline{1,m} \\ |u_\infty(\hat{\mathbf{x}}_j) - f_{\infty,j}| \leqslant \mu & \text{for } j = \overline{1,n} \end{cases} .$$

Hence, from the remark 3.4 we deduce that the control problem (1)–(3) amounts to to finding the density $w \in L^2(\partial D'_a)$ so that the corresponding solution u of (1), (3) and its corresponding far-field pattern u_∞ satisfy

$$\begin{cases} \|u - f\|_{L^2(\bigcup_{l=1}^m \partial W_l)} \leqslant \mu \\ |u_\infty(\hat{\mathbf{x}}_j) - f_{\infty,j}| \leqslant \mu & \text{for } j = \overline{1,n} \end{cases} \tag{13}$$

for any $f = (f_1, f_2, \ldots, f_m) \in Y$ and fixed directions $\hat{\mathbf{x}}_j$, $j = \overline{1,n}$. The second constraint in (13) is an added novelty to our work, as we consider the far-field pattern in certain prescribed and *a priori* fixed far-field directions $(\hat{\mathbf{x}}_1, \hat{\mathbf{x}}_2, \ldots, \hat{\mathbf{x}}_n)$. We model the far-field pattern in these far-field directions by using the far-field pattern operator $\mathcal{K}_\infty : L^2(\partial D'_a) \to \mathbb{C}^n$ defined as

$$\mathcal{K}_\infty w = \left(\mathcal{P}_{w,1}, \mathcal{P}_{w,2}, \ldots, \mathcal{P}_{w,n}\right)$$

where for each $j = \overline{1,n}$,

$$\mathcal{P}_{w,j} = \frac{1}{4\pi}\int_{\partial D'_a} w(\mathbf{y})e^{-ik\hat{\mathbf{x}}_j \cdot \mathbf{y}}dS_{\mathbf{y}}. \tag{14}$$

Hence, the overall propagator operator $\mathcal{D} : L^2(\partial D'_a) \to Y \times \mathbb{C}^n$ is defined such that

$$\mathcal{D}w(\mathbf{y}_1, \ldots, \mathbf{y}_m) = \left(\mathcal{K}_1 w(\mathbf{y}_1), \ldots, \mathcal{K}_m w(\mathbf{y}_m), \mathcal{P}_{w,1}, \mathcal{P}_{w,2}, \ldots, \mathcal{P}_{w,n}\right). \tag{15}$$

where $\mathbb{C}^n$ is endowed with the usual dot product and where $Y \times \mathbb{C}^n$ is described by the usual graph metric,

$$\langle u, v\rangle_{Y\times\mathbb{C}^n} = \langle f, g\rangle_Y + \sum_{i=1}^n c_i \cdot \overline{d}_i$$

for $u = (f, c_1, c_2, \ldots, c_n)$, $v = (g, d_1, d_2, \ldots, d_n) \in Y \times \mathbb{C}^n$. To show the existence of a solution to the control problem (1), (3), (13) we show that the linear compact propagator operator $\mathcal{D}$

has a dense range. This is established in the following theorem by showing that the adjoint operator $\mathcal{D}^*$ has a trivial kernel.

Theorem 3.1. *Except a discrete set of values for k, the operator $\mathcal{D}$ defined in (15) has a dense range.*

Proof. We prove the equivalent assertion that the adjoint $\mathcal{D}^*$ has a trivial kernel. We first note that by simple algebraic manipulation one can obtain that the adjoint operator $\mathcal{D}^* : Y \times \mathbb{C}^n \to L^2(\partial D'_a)$ is given by

$$\left(\mathcal{D}^*(\psi, c)\right)(\mathbf{y}) = \sum_{l=1}^{m} \mathcal{K}_l^* \psi_l(\mathbf{y}) + \sum_{j=1}^{n} \frac{c_j \, e^{ik\hat{\mathbf{x}}_j \cdot \mathbf{y}}}{4\pi}, \tag{16}$$

for any $\psi = (\psi_1, \psi_2, \ldots, \psi_m) \in Y$, $c = (c_1, c_2, \ldots, c_n) \in \mathbb{C}^n$ and $\mathbf{y} \in \partial D'_a$ where the operator $\mathcal{K}_l^* : L^2(\partial W_l) \to L^2(\partial D'_a)$ is given by

$$\mathcal{K}_l^* \psi_l(\mathbf{y}) = \int_{\partial W_l} \psi_l(\mathbf{x}) \overline{\phi}(\mathbf{x}, \mathbf{y}) dS_{\mathbf{x}}, \tag{17}$$

for $l = \overline{1, m}$. Suppose $(\psi, c) \in \ker \, \mathcal{D}^*$, i.e.,

$$\left(\mathcal{D}^*(\psi, c)\right)(\mathbf{y}) = \sum_{l=1}^{m} \mathcal{K}_l^* \psi_l(\mathbf{y}) + \sum_{j=1}^{n} \frac{c_j \, e^{ik\hat{\mathbf{x}}_j \cdot \mathbf{y}}}{4\pi} = 0 \tag{18}$$

for any $\mathbf{y} \in \partial D'_a$. Define $w(\mathbf{y}) = \sum_{l=1}^{m} \int_{\partial W_l} \overline{\psi}_l(\mathbf{x}) \phi(\mathbf{x}, \mathbf{y}) dS_{\mathbf{x}} + \sum_{j=1}^{n} \frac{\overline{c}_j \, e^{-ik\hat{\mathbf{x}}_j \cdot \mathbf{y}}}{4\pi}$, where the integrals exists as improper integrals on the ∂W_l's. Note that each term in w is a solution of the Helmholtz equation and so together with (18), we have

$$\begin{cases} \Delta w + k^2 w = 0 & \text{in } D'_a \\ w = 0 & \text{on } \partial D'_a \end{cases}. \tag{19}$$

Proceeding as in [39], by using analytic continuation, $w = 0$ in D'_a and then by the continuity of the single layer potential together with the uniqueness of the interior problem in each of the regions $\{W_l\}_{l=1}^{m}$ we obtain that $w = 0$ on $\mathbb{R}^3$. Finally, classical interior and exterior jump relations for the single layer potential on the ∂W_l's imply $\psi_l = 0$ on ∂W_l, $l = \overline{1, m}$. This, when used in (18) gives

$$\sum_{j=1}^{n} c_j \, e^{ik\hat{\mathbf{x}}_j \cdot \mathbf{y}} = 0 \tag{20}$$

for any $\mathbf{y} \in \mathbb{R}^3$. We seek to show that $c_j = 0$ for $j = \overline{1, n}$. Fix a $\hat{\mathbf{y}}_0 \in \mathbb{R}^3$ and define $\mathbf{y}_p = p\hat{\mathbf{y}}_0$ for $p = \overline{0, n-1}$. Plugging-in $\mathbf{y} = \mathbf{y}_p$ in (20) yields the $n \times n$ system

$$c_1 + c_2 + \cdots + c_n = 0$$

$$c_1 \, e^{ik\hat{\mathbf{x}}_1 \cdot \mathbf{y}_1} + c_2 \, e^{ik\hat{\mathbf{x}}_2 \cdot \mathbf{y}_1} + \cdots + c_n \, e^{ik\hat{\mathbf{x}}_n \cdot \mathbf{y}_1} = 0$$

$$\vdots \tag{21}$$

$$c_1 \, e^{ik\hat{\mathbf{x}}_1 \cdot \mathbf{y}_{n-1}} + c_2 \, e^{ik\hat{\mathbf{x}}_2 \cdot \mathbf{y}_{n-1}} + \cdots + c_n \, e^{ik\hat{\mathbf{x}}_n \cdot \mathbf{y}_{n-1}} = 0.$$

Let $\mathbf{z}_j = e^{ik\hat{\mathbf{x}}_j \cdot \hat{\mathbf{y}}_0}$. Then (21) can be written as a Vandermonde system

$$\begin{bmatrix} 1 & 1 & \cdots & 1 \\ z_1 & z_2 & \cdots & z_n \\ & & \vdots & \\ z_1^{n-1} & z_2^{n-1} & \cdots & z_n^{n-1} \end{bmatrix} \begin{bmatrix} c_1 \\ c_2 \\ \vdots \\ c_n \end{bmatrix} = \begin{bmatrix} 0 \\ 0 \\ \vdots \\ 0 \end{bmatrix}. \tag{22}$$

This system admits a unique solution (the trivial solution $c_j = 0$ for all $j = \overline{1, n}$) unless the coefficient matrix has determinant zero. Note that

$$\det\left(\begin{bmatrix} 1 & 1 & \cdots & 1 \\ z_1 & z_2 & \cdots & z_n \\ & & \vdots & \\ z_1^{n-1} & z_2^{n-1} & \cdots & z_n^{n-1} \end{bmatrix}\right) = \prod_{1 \leqslant j < l \leqslant n} (z_j - z_l),$$

which is zero if and only if there are indices q_1 and q_2 such that $z_{q_1} = z_{q_2}$, or equivalently, if and only if

$$(\hat{\mathbf{x}}_{q_1} - \hat{\mathbf{x}}_{q_2}) \cdot \hat{\mathbf{y}}_0 = \frac{2\pi}{k} M \tag{23}$$

for some integer M. By the triangle and the Cauchy–Schwarz inequalities we obtain

$$|M| = \frac{k}{2\pi}|(\hat{\mathbf{x}}_{q_1} - \hat{\mathbf{x}}_{q_2}) \cdot \hat{\mathbf{y}}_0| \leqslant \frac{k}{\pi}. \tag{24}$$

Thus, choosing $\hat{\mathbf{y}}_0$ outside of the finite number of hyperplanes defined by the $\binom{n}{2}\left(2\left\lfloor\frac{k}{\pi}\right\rfloor + 1\right)$ equations of the form (23), will give rise to a set of n **y**-values (i.e., $\mathbf{y}_p = p\hat{\mathbf{y}}_0$ for $p = \overline{0, n-1}$) forcing the solution $c = (c_1, c_2, \ldots, c_n)$ of (20) to satisfy $c_j = 0$ for all $j = \overline{1, n}$. Therefore, the kernel of $\mathcal{D}^*$ is trivial and so $\mathcal{D}$ has a dense range. $\qquad\square$

3.2. Numerical simulations

In this section we present several numerical simulations supporting the theoretical results presented above. We further develop the scheme proposed in [11, 39, 40] to accommodate the added constraints on the radiated far-field pattern. For a given $f = (f_1, f_2, \ldots, f_m) \in Y$ and far-field pattern values $c = (c_1, c_2, \ldots, c_n) \in \mathbb{C}^n$, the problem is to find $w \in L^2(\partial D'_a)$ such that

$$\mathcal{D}w \approx f \times c. \tag{25}$$

To solve (25), we employ a method of moments approach by discretizing the control regions into a mesh of collocation points and writing the density w in terms of local basis functions as in [12] (see also [10, 44]). Hence, the problem is reduced to a linear system of the form

$$Aw_d \approx b, \tag{26}$$

where A is the coefficient matrix of dimensions $N_r \times N_c$ where N_r is the total number of mesh points in all near controls and far-field directions and N_c is the number of local basis functions used in representing w. The vector w_d of the discrete unknown coefficients of w is computed as the Tikhonov solution
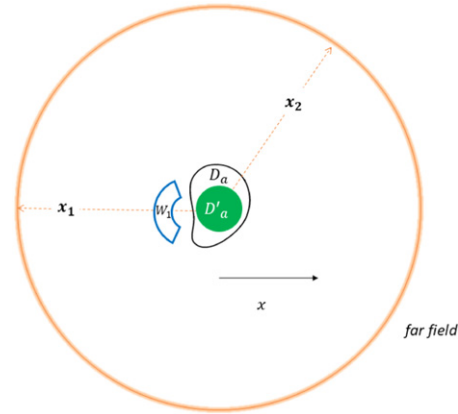
$$w_d = (\alpha I + A^*A)^{-1}A^*b \tag{27}$$

Figure 1. Sketch of the top view (plane $z = 0$) of the problem geometry showing the near control W_1 and the far-field directions $\mathbf{x_1}$ and $\mathbf{x_2}$.

for some optimal regularization parameter $0 < \alpha \ll 1$ calculated using the Morozov discrepancy principle, where A^* denotes the complex conjugate transpose of A (see [40]).

　　In the following simulations the fictitious source domain D'_a is a sphere of radius 0.01 m centered at the origin while for simplicity, the physical source domain D_a is chosen to be the sphere of radius 0.015 m centered at the origin (though in general, it can be any Lipschitz compact domain with $D'_a \Subset D_a$ which does not intersect the near-field control regions). We consider the control problem in which the far-field direction $\hat{\mathbf{x}}_1$ is situated behind a near field. We consider two cases: first, when we prescribe a null in the near field control region W_1, hence mimicking communications through an obstacle and second, when the near field is the outgoing plane wave $f(\mathbf{x}) = e^{i\mathbf{x}\cdot(10\mathbf{d})}$ with $\mathbf{d} = [-1, 0, 0]$, simulating covert communication. The unknown density is defined on $\partial D'_a$ by using 234 local basis functions. The near control is the annular sector

$$W_1 = \left\{ (r, \theta, \phi) : r \in [0.02, 0.03], \theta \in \left[\frac{\pi}{4}, \frac{3\pi}{4}\right], \phi \in \left[\frac{3\pi}{4}, \frac{5\pi}{4}\right] \right\}$$

in spherical coordinates with respect to the origin where r is the radius, $\theta \in [0, \pi]$ is the inclination angle and $\phi \in [0, 2\pi)$ is the azimuthal angle. This sector is discretized into 4640 points. The far-field directions in Cartesian coordinates are $\hat{\mathbf{x}}_1 = [-1, 0, 0]$, directly behind the near control and $\hat{\mathbf{x}}_2 = \left[\frac{1}{2}, \frac{1}{2}, -\frac{\sqrt{2}}{2}\right]$. The problem geometry is shown in figure 1. To check the accuracy of the generated fields, we provide the plots of the prescribed and generated near fields and when applicable the pointwise relative error. As a further numerical stability check, these fields were plotted in a mesh of points slightly off the set of points used in the collocation scheme. Then aside from stating the generated far-field pattern and the relative error, whenever applicable, on the directions $\hat{\mathbf{x}}_1$ and $\hat{\mathbf{x}}_2$ we also present the generated far-field pattern on a small patch around the two directions. The computed normal velocity on the physical source domain is characterized in two-dimensional $\theta\phi$-plots of its magnitude and real and imaginary parts. We also calculate the average radiated power by the source given by

$$P_{\text{ave}} = \frac{1}{2} \int_{\partial B_r(\mathbf{0})} \text{Re} \left[\overline{u}(\nabla u \cdot \mathbf{n}) \right] \mathrm{d}S \tag{28}$$
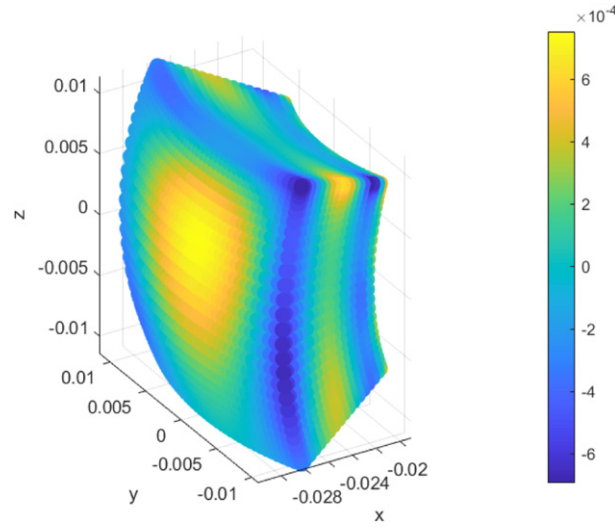
Figure 2. Real part of the generated near field.

where $\partial B_r(\mathbf{0})$ is the surface of any sphere containing the source and in our calculations we will evaluate the power in dB relative to a reference level of 10^{-12} W.

3.2.1. A null near field. In this test, we simulate the case of communicating while avoiding an obstacle and keeping a low signature in another far-field direction. We prescribe a null field in W_1 and the pair of far-field pattern values 0.01 and 0 in the directions of $\hat{\mathbf{x}}_1$ and $\hat{\mathbf{x}}_2$, respectively. Figure 2 shows the generated field on the near control. The field on the near control region has maximum pointwise magnitude of about 8×10^{-4}.

Figure 3 shows the generated far-field pattern values on the two directions. These plots suggest a good approximation of the far-field values even on the patches around $\hat{\mathbf{x}}_1$ and $\hat{\mathbf{x}}_2$. The generated pattern value for $\hat{\mathbf{x}}_1$ is approximately $0.009\,98 + 5.83 \times 10^{-6}$ i, with a relative error of only about 0.22%. Meanwhile the generated value on $\hat{\mathbf{x}}_2$ is $-1.5711 \times 10^{-6} -5.84 \times 10^{-6}$ i.

The computed normal velocity on the physical source is characterized in figure 4. Here, we see that these values has magnitudes values of order 10^{-3}. The average power radiated by the source is approximately 5.80×10^{-4} or around 87.63 dB.

3.2.2. A plane wave in the near field. In this experiment, we synthesize a plane wave on the near control while keeping the direction behind it a quiet zone and projecting a pattern in another far-field direction. We prescribe the left traveling plane wave $f(\mathbf{x}) = \mathrm{e}^{\mathrm{i}\mathbf{x}\cdot(10\mathbf{d})}$ with $\mathbf{d} = [-1, 0, 0]$ on the near control, a zero far-field pattern value in the direction $\hat{\mathbf{x}}_1$ behind it and 0.01 in the direction $\hat{\mathbf{x}}_2$. The results of the near-field approximation is shown in figure 5. The near-field relative errors do not exceed 1.5%.

The results of the far-field pattern synthesis are shown in figure 6. The results on the patch around $\hat{\mathbf{x}}_1$ are good, with generated values of order 10^{-4}. In particular, the generated value at $\hat{\mathbf{x}}_1$ is around $2.6 \times 10^{-4} - 1.02 \times 10^{-4}$ i. Meanwhile on the patch around $\hat{\mathbf{x}}_2$, there are points where the relative error reach 22%. But this decreases to desirable values for points near $\hat{\mathbf{x}}_2$. In fact, the generated value at $\hat{\mathbf{x}}_2$ is $0.010\,04 + 2.78 \times 10^{-5}$ i with a relative error of just about 0.021%.

Lastly, we look at the calculated normal velocity. Figure 7 displays the pointwise magnitude as well as the real and imaginary parts of the normal velocity on the physical source. The
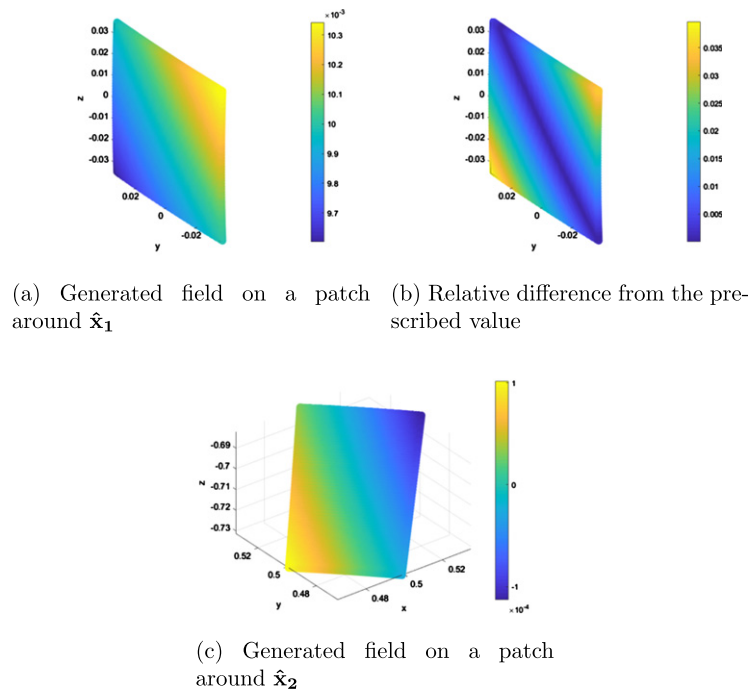
(a) Generated field on a patch around $\hat{\mathbf{x}}_1$

(b) Relative difference from the prescribed value

(c) Generated field on a patch around $\hat{\mathbf{x}}_2$

Figure 3. Results of the far-field pattern directional control.
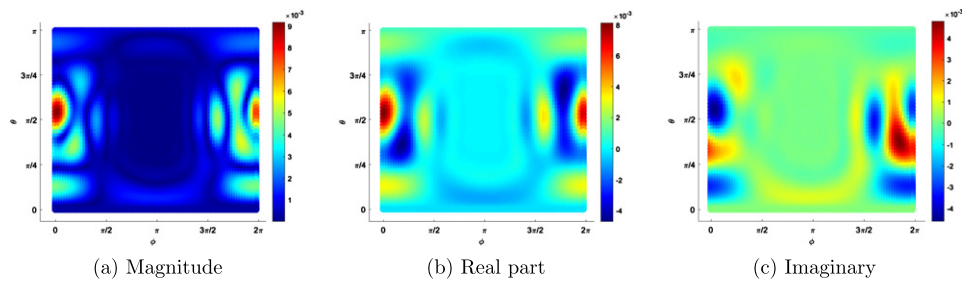

(a) Magnitude

(b) Real part

(c) Imaginary

Figure 4. The computed normal velocity on the actual source.

average acoustic power radiated by the source is around 2.44×10^{-2} or about 103.87 dB which, as expected is larger than in the previous simulations due to the extra work the source needs to do now to create a plane wave in the near-field control region.

4. Homogeneous ocean environment

In this section, we prove the possibility of near-field active control while maintaining desired radiation in prescribed far-field directions in a homogeneous ocean environment of constant depth. The problem is similar to the one presented in section 3 except that the sources and the control regions are submerged in a homogeneous ocean environment. The near-field control problem was briefly discussed in [40] without numerical simulations. Aside from providing numerical validation, this section adds the novelty of incorporating additional far-field pattern
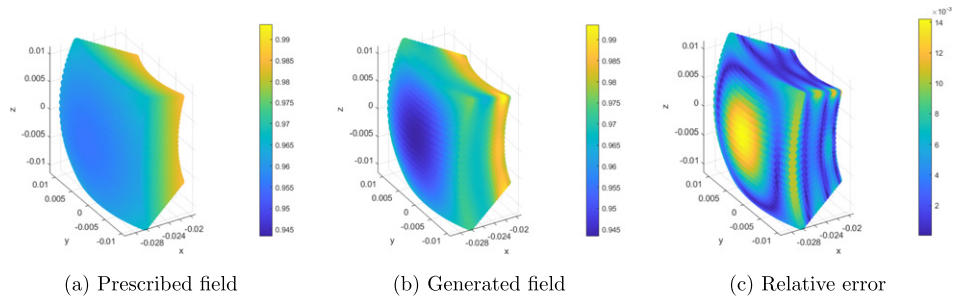
(a) Prescribed field　　　　(b) Generated field　　　　(c) Relative error

Figure 5. Results of the field synthesis on the near control.

(a) Generated field on a patch around $\hat{\mathbf{x}}_1$

(b) Generated field on a patch around $\hat{\mathbf{x}}_2$
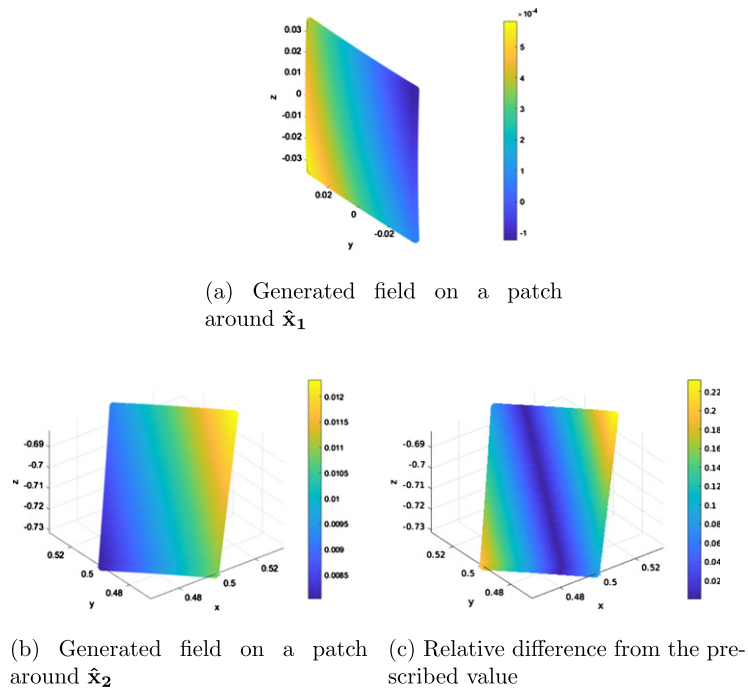
(c) Relative difference from the prescribed value

Figure 6. Results of the far-field pattern directional control.

constraints in the theoretical analysis which is an important feature from the point of view of applications and theoretically nontrivial in this particular environment.

Assuming the same notations as in the theoretical set-up of section 3 the problem is modeled by (1), (2) with the boundary conditions (4)

$$\begin{cases} u = 0 \text{ at the ocean surface } z = 0 \text{ and} \\ \dfrac{\partial u}{\partial z} = 0 \text{ at the ocean floor } z = h. \end{cases} \qquad (29)$$

and the radiation condition described below at (33). A sketch of the geometry is shown in figure 8. We continue with the presentation of the theoretical framework and results. Then we
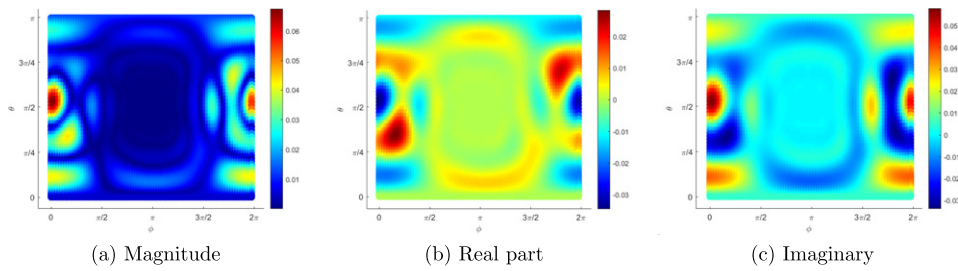
(a) Magnitude   (b) Real part   (c) Imaginary

Figure 7. The computed normal velocity on the actual source.
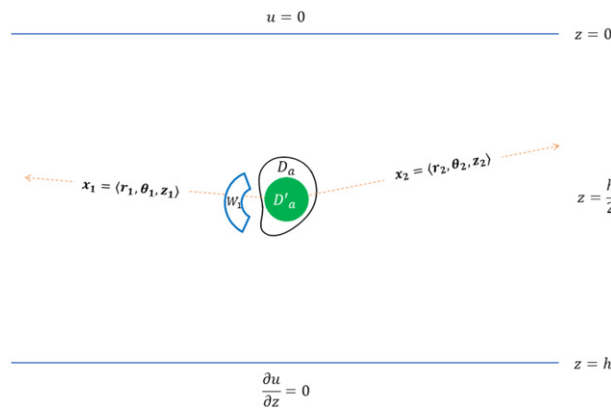

Figure 8. A 3D sketch of the problem geometry for the homogeneous ocean showing the near control and two far-field directions $\mathbf{x_1}$ and $\mathbf{x_2}$.

perform some numerical simulations that illustrate the feasibility of the proposed theoretical and numerical framework.

4.1. Theoretical framework

The mathematical and numerical framework from our previous works can be adapted for the homogeneous ocean environment. In this section we will assume that the entire functional framework (notations, geometrical conditions and functional assumptions) formulated in section 2 remains the same for the case of homogeneous oceans of constant depth unless otherwise specified. The major adjustment is the Green's function for this new medium. The corresponding Green's function for this environment has the normal mode representation for an evaluation point $\mathbf{x} = (r, \theta, z)$ and source point $\mathbf{y} = (0, \theta_0, z_0)$ in cylindrical coordinates

$$G(\mathbf{x}, \mathbf{y}) = \frac{i}{2h} \sum_{p=0}^{+\infty} \phi_p(z) \phi_p(z_0) H_0^{(1)}(ka_p r) \tag{30}$$

where $H_0^{(1)}$ is the Hankel function of order zero of the first kind, ϕ_p is the pth modal solution with associated eigenvalue a_p (see [2, 22, 25]). These eigenpairs are given by

$$a_p = \sqrt{1 - \frac{(2p+1)^2\pi^2}{4k^2h^2}} \quad \text{and} \tag{31}$$

$$\phi_p(z) = \sin\left(k\sqrt{1-a_p^2}z\right) = \sin\left(\frac{(2p+1)\pi}{2h}z\right). \tag{32}$$

As proved in [2], the function G can be expressed as a continuous perturbation of the Green's function in free space. We will assume that the physical source D_a satisfy $\mathbf{x} \cdot \mathbf{n} \geqslant 0$ for any $\mathbf{x} \in \partial D_a$ where $\mathbf{n}$ denotes the exterior normal to $\mathbf{x} \in \partial D_a$.

With these notations, the forward problem in the homogeneous finite-depth ocean environment $R = \{\mathbf{x} = (r, \theta, z) \in \mathbb{R}^3 | z \in [h, 0]\}$ can be formulated as follows: for a given boundary input u_b on the surface of the source ∂D_a find u solution of the following exterior Helmholtz problem

$$\begin{cases} \Delta u + k^2 u = 0 \text{ in } R \backslash D_a, \\ u = u_b \text{ on } \partial D_a \\ u = 0 \text{ at the ocean surface } z = 0 \text{ and} \\ \dfrac{\partial u}{\partial z} = 0 \text{ at the ocean floor } z = h \\ \lim_{r\to\infty} r^{1/2}\left(\dfrac{\partial u_p}{\partial r} - ika_p u_p\right) = 0, \quad \text{uniformly for all } \theta \in [0, 2\pi), \end{cases} \tag{33}$$

where u_p in the radiation condition above are normal modes appearing in the representation of the solution u, i.e.,

$$u(\mathbf{x}) = \sum_{p=0}^{\infty} \phi_p(z)u_p(r, \theta), \quad \text{for large enough } r. \tag{34}$$

Classical manipulations and the definition of the Green's function introduced at (30) imply that, for any density $w \in C(\partial D_a')$, the following function

$$u(\mathbf{x}) = \int_{\partial D_a'} w(\mathbf{y})G(\mathbf{x}, \mathbf{y})dS_{\mathbf{y}} \tag{35}$$

is a solution to (33) with $u_b \in C^\infty(\partial D_a)$ given by $u_b = \int_{\partial D_a'} w(\mathbf{y})G(\mathbf{x}, \mathbf{y})dS_{\mathbf{y}}$. Note that, as before, we make use of a fictitious spherical source domain D_a' to ensure smoothness of our boundary input u_b. It was shown in [2] that for a given density $w \in \partial D_a'$, u defined above has an asymptotic representation given by

$$u(\mathbf{x}) = \sum_{p=0}^{N} \frac{1}{\sqrt{ka_p r}} e^{ika_p r}g_p(\theta, z) + \mathcal{O}\left(\frac{1}{r^{3/2}}\right), \quad \text{as } r \to +\infty \tag{36}$$

where $\mathbf{x} = (r, \theta, z)$ (in cylindrical coordinates) and for each $p = \overline{0, N}$ and $\mathbf{y} = (r', \theta', z') \in \partial D_a'$ in cylindrical coordinates,

$$g_p(\theta, z) = \sqrt{\frac{2}{\pi}} \int_{\partial D_a'} w(\mathbf{y}) \left(\sum_{q=0}^{\infty} e^{-i(q+\frac{1}{2})\frac{\pi}{2}}\alpha_{qp}(z, \theta, r', z', \theta')\right) dS_{\mathbf{y}} \tag{37}$$

and

$$\alpha_{qp}(z, \theta, r', z', \theta') = \frac{i\epsilon_q}{2h} \phi_p(z) \left[\cos(q\theta)\beta_{qp}(\mathbf{y}) + \sin(q\theta)\gamma_{qp}(\mathbf{y})\right] \tag{38}$$

where $\epsilon_0 = 1$, and $\epsilon_q = 2$ for $q \geqslant 1$ and where

$$\beta_{qp}(\mathbf{y}) = J_q(ka_p r')\phi_p(z') \cos q\theta' \text{ and} \tag{39}$$

$$\gamma_{qp}(\mathbf{y}) = J_q(ka_p r')\phi_p(z') \sin q\theta'. \tag{40}$$

In the last two equations above J_q is the Bessel function of the first kind of order q. Then following [2] we define the far-field pattern as the function u_∞ given by

$$u_\infty(\hat{\mathbf{x}}) = \sum_{p=0}^{N} g_p(\theta, z), \tag{41}$$

where $\hat{\mathbf{x}} = (1, \theta, z)$ and $N > \frac{kh}{\pi} - \frac{1}{2}$ so that the terms g_p removed from the sum are all evanescent (non-propagating) modes.

Remark 4.1. The restriction that each f_l satisfies the Helmholtz equation in some neighborhood of R_l and the fact that $R_l \Subset W_l$ for all $1 \leqslant l \leqslant m$ ensure, through uniqueness and regularity results for the interior Helmholtz problems (in the spirit of [39]), that the field u, solution of (33), will satisfy the control constraint (2) if

$$\begin{cases} \|u - f_l\|_{L^2(\partial W_l)} \leqslant \mu & \text{for } l = \overline{1, m} \\ |u_\infty(\hat{\mathbf{x}}_j) - f_{\infty,j}| \leqslant \mu & \text{for } j = \overline{1, n} \end{cases}.$$

Hence, from the remark 4.1 we deduce that the control problem (33), (2) amounts to to finding the density $w \in L^2(\partial D_a')$ so that the corresponding solution u of (33) and its corresponding far-field pattern u_∞ satisfy

$$\begin{cases} \|u - f\|_{L^2(\bigcup_{l=1}^m \partial W_l)} \leqslant \mu \\ |u_\infty(\hat{\mathbf{x}}_j) - f_{\infty,j}| \leqslant \mu & \text{for } j = \overline{1, n} \end{cases} \tag{42}$$

for any $f = (f_1, f_2, \ldots, f_m) \in Y$ and fixed directions $\hat{\mathbf{x}}_j$, $j = \overline{1, n}$. Such a density will give us then the necessary source presure characterization $u_b = \int_{\partial D_a'} w(\mathbf{y})G(\mathbf{x}, \mathbf{y})dS_{\mathbf{y}}$ on the physical source D_a so that its radiated field satisfies the required control conditions (2).

Because the control problem is again reduced to finding the density on the surface of the fictitious source D_a' we note that the same machinery developed in the previous section can be employed after the making the appropriate modification of the Green's function.

In parallel to the notations in the previous section, we define the near-field propagator operator $\mathcal{K} : L^2(\partial D_a') \to Y$, by

$$\mathcal{K}w(\mathbf{y}_1, \mathbf{y}_2, \ldots, \mathbf{y}_m) = \left(\mathcal{K}_1 w(\mathbf{y}_1), \mathcal{K}_2 w(\mathbf{y}_2), \ldots, \mathcal{K}_m w(\mathbf{y}_m)\right) \tag{43}$$

where for each $l = \overline{1, m}$, $\mathbf{y}_l \in W_l$

$$\mathcal{K}_l w(\mathbf{y}_l) = \int_{\partial D_a'} w(\mathbf{x})G(\mathbf{x}, \mathbf{y}_l)dS_{\mathbf{x}}. \tag{44}$$

and for each far-field direction with cylindrical coordinates $\hat{\mathbf{x}}_j = (1, \theta_j, z_j)$, $j = \overline{1, n}$ with $z_j \in (h, 0)$, $\theta_j \in [0, 2\pi)$ and $\theta_{j_1} \neq \theta_{j_2}$ for $j_1 \neq j_2$, we define the far-field pattern propagator $\mathcal{K}_\infty : L^2(\partial D'_a) \to \mathbb{C}^n$ as

$$\mathcal{K}_\infty w = \left(\mathcal{P}_{w,1}, \mathcal{P}_{w,2}, \ldots, \mathcal{P}_{w,n} \right)$$

where

$$\mathcal{P}_{w,j} = \sum_{p=0}^{N} g_p(\theta_j, z_j). \tag{45}$$

Finally, we define the operator $\mathcal{D} : L^2(\partial D'_a) \to Y \times \mathbb{C}^n$ such that

$$\mathcal{D}w(\mathbf{y}_1, \ldots, \mathbf{y}_m) = \left(\mathcal{K}_1 w(\mathbf{y}_1), \ldots, \mathcal{K}_m w(\mathbf{y}_m), \mathcal{P}_{w,1}, \mathcal{P}_{w,2}, \ldots, \mathcal{P}_{w,n} \right). \tag{46}$$

To prove that the range of the linear compact operator $\mathcal{D}$ is dense in $Y \times \mathbb{C}^n$, i.e., any target in $Y \times \mathbb{C}^n$ can be approximated by an image under $\mathcal{D}$, we shall show in the next theorem that the adjoint operator $\mathcal{D}^*$ has a trivial kernel.

Theorem 4.1. *Except a discrete set of values for k, the operator $\mathcal{D}$ defined in (46) has a dense range.*

Proof. Again, we prove the equivalent statement that $\mathcal{D}^*$ has a trivial kernel. To do so, we adapt the arguments used in the proof of theorem 3.1. Straightforward calculations will show that the adjoint operator $\mathcal{D}^* : Y \times \mathbb{C}^n \to L^2(\partial D'_a)$ is given by

$$(\mathcal{D}^*(\psi, c))(\mathbf{y}) = \sum_{l=1}^{m} \mathcal{K}_l^* \psi_l(\mathbf{y}) + \sum_{j=1}^{n} c_j h_j(\mathbf{y}), \tag{47}$$

where $\mathcal{K}_l^* : L^2(\partial W_l) \to L^2(\partial D'_a)$ is given by

$$\mathcal{K}_l^* \psi_l(\mathbf{y}) = \int_{\partial W_l} \psi_l(\mathbf{x}) \overline{G}(\mathbf{x}, \mathbf{y}) dS_{\mathbf{x}}.$$

for any $\mathbf{y} \in \partial D'_a$ and $h_j : \partial D'_a \to \mathbb{C}$ is defined as

$$h_j(\mathbf{y}) = \sqrt{\frac{2}{\pi}} \sum_{p=0}^{N} \sum_{q=0}^{\infty} e^{i(q+\frac{1}{2})\frac{\pi}{2}} \overline{\alpha}_{qp}(z_j, \theta_j, \mathbf{y}).$$

Consider $(\psi, c) \in Y \times \mathbb{C}^n$ with $(\mathcal{D}^*(\psi, c)) = 0$. Let

$$w(\mathbf{y}) = \int_{\partial W_l} \overline{\psi}_l(\mathbf{x}) G(\mathbf{x}, \mathbf{y}) dS_{\mathbf{x}} + \sum_{j=1}^{n} \overline{c}_j \overline{h}_j(\mathbf{y}), \tag{48}$$

It is simple to observe that w defined in (48) is a solution of the interior Helmholtz equation in D'_a with zero Dirichlet data on the boundary (since by definition $\mathcal{D}^*(\psi, c) = 0$), and except a finite set of values for k this implies that $w = 0$ in D'_a. Next, in the same spirit as we did for the case of free space environments in the previous section, using analytic continuation and the same continuity and jump relations for the single layer potential used in the proof of theorem 3.1 (which still apply since G is a continuous perturbation of the Green's function in free space), we discern that $w(\mathbf{y}) = 0$, for $\mathbf{y} \in R$. This, and the jump conditions for the single

layer potential (which still apply since G is a continuous perturbation of the Green's function in free space) imply $\psi_l = 0$ on $\partial W_l, l = \overline{1, m}$. Thus, using this in $w(\mathbf{y}) = 0$, for $\mathbf{y} \in R$ recalling (48) we obtain the following condition for $c = (c_1, c_2, \ldots c_n)$:

$$\sum_{j=1}^{n}\sum_{p=0}^{N}\sum_{q=0}^{\infty}\overline{c}_j \, \mathrm{e}^{-i(q+\frac{1}{2})\frac{\pi}{2}}\alpha_{qp}(z_j, \theta_j, \mathbf{y}) = 0 \quad \text{for any } \mathbf{y} \in R. \tag{49}$$

To prove that the kernel of $\mathcal{D}^*$ is trivial it remains to show that (49) implies that all c_j's are zero. Let q_0 with $0 \leqslant q_0 < \infty$ be arbitrarily fixed. Taking the inner product of both sides of (49) against $\cos q_0\theta'$, applying the orthogonality property of sines and cosines and algebraic manipulations yields for any $\mathbf{y} = (r', \theta', z') \in R$

$$\sum_{j=1}^{n}\sum_{p=0}^{N}\overline{c}_j\phi_p(z_j)J_{q_0}(ka_pr')\phi_p(z')\cos(q_0\theta_j) = 0. \tag{50}$$

Note that

$$\frac{\mathrm{d}^{(l)}}{\mathrm{d}z'}\phi_p(0) = \begin{cases} 0, & \text{if } l \text{ is even} \\ k^l(1 - a_p^2)^{l/2}, & \text{for } l = 1, 5, 9, \ldots. \\ -k^l(1 - a_p^2)^{l/2}, & \text{for } l = 3, 7, 11, \ldots \end{cases}$$

Define $A_p = \sum_{j=1}^{n}\overline{c}_j\phi_p(z_j)\cos(q_0\theta_j)$ and let $B_p = k(1 - a_p^2)^{1/2}$. Taking the the order $l = 1 + 4s$ derivative of both sides of (50) with respect to z' evaluated at $z' = 0$, one obtains the system

$$\sum_{p=0}^{N}A_pJ_{q_0}(ka_pr')B_p^{1+4s} = 0, s = \overline{0, N}. \tag{51}$$

Letting $\lambda_p = B_p^4$, system (51) can be viewed as an $N + 1 \times N + 1$ system with unknowns A_pB_p with coefficient matrix

$$D = \begin{bmatrix} J_{q_0}(ka_0r') & J_{q_0}(ka_1r') & \cdots & J_{q_0}(ka_Nr') \\ J_{q_0}(ka_0r')\lambda_0 & J_{q_0}(ka_1r')\lambda_1 & \cdots & J_{q_0}(ka_Nr')\lambda_N \\ & & \vdots & \\ J_{q_0}(ka_0r')\lambda_0^N & J_{q_0}(ka_1r')\lambda_1^N & \cdots & J_{q_0}(ka_Nr')\lambda_N^N \end{bmatrix} \tag{52}$$

with det $D = \left(\prod_{p=0}^{N}J_{q_0}(ka_pr')\right)\left(\prod_{1\leqslant p<l\leqslant n}(\lambda_p - \lambda_l)\right)$. Note that by definition $\lambda_p - \lambda_l \neq 0$ for $p \neq l$. From [1], the smallest root of J_{q_0} is bounded below by $q_0 + \frac{2}{3}|\xi|^{3/2}$, where $\xi = -0.366\,05\ldots$ is the smallest negative root of the Airy function. Since the a_p's are decreasing then choosing r' so that

$$r' < \frac{q_0 + \frac{2}{3}|\xi|^{3/2}}{ka_0}$$

makes det$D \neq 0$. Hence, (51) only has the trivial solution $A_pB_p = 0$ for all $p = \overline{0, N}$ implying

$$\sum_{j=1}^{n}\overline{c}_j\phi_p(z_j)\cos(q_0\theta_j) = 0. \tag{53}$$

On the other hand, taking the inner product of both sides of (49) against $\sin q_0 \theta'$ and doing analogous calculations as above yields

$$\sum_{j=1}^{n} \overline{c}_j \phi_p(z_j) \sin(q_0 \theta_j) = 0 \tag{54}$$

for all $p = \overline{0, N}$. In particular for $p = 0$, the last two equations imply

$$\sum_{j=1}^{n} \overline{c}_j \phi_0(z_j) e^{iq_0 \theta_j} = 0. \tag{55}$$

Since q_0 was arbitrarily chosen, by using the values $q_0 = 0, 1, \ldots, n-1$ above we obtain the following homogeneous linear system of equations in unknowns $\overline{c}_j$ with coefficient matrix

$$E = \begin{bmatrix} \phi_0(z_1) & \phi_0(z_2) & \cdots & \phi_0(z_n) \\ \phi_0(z_1)e^{i\theta_1} & \phi_0(z_2)e^{i\theta_2} & \cdots & \phi_0(z_n)e^{i\theta_n} \\ & & \vdots & \\ \phi_0(z_1)e^{i(n-1)\theta_1} & \phi_0(z_2)e^{i(n-1)\theta_2} & \cdots & \phi_0(z_n)e^{i(n-1)\theta_n} \end{bmatrix}. \tag{56}$$

Note that E is another Vandermonde-type matrix with determinant

$$\det \ E = \left(\prod_{j=1}^{n} \phi_0(z_j) \right) \left(\prod_{1 \leqslant q < l \leqslant n} (e^{i\theta_q} - e^{i\theta_l}) \right).$$

This will be zero if and only if there exists a z_j such that $\phi_0(z_j) = 0$ or equivalently, $z_j = 2nd$ for some integer t. However, this cannot be the case since $z_j \in (h, 0)$. Hence, (55) has a unique solution, namely $c_j = 0, \quad j = \overline{1, n}$. Therefore, ker $\mathcal{D}^*$ is trivial and consequently, $\mathcal{D}$ has a dense range. $\qquad \square$

4.2. Numerical simulations

In this section we present numerical simulations illustrating the results obtained in section 4.1. The numerical framework is an adaptation of the one discussed in section 3.2 where the calculation of the matrix of moments is modified with the corresponding Green's function and far-field pattern for the homogeneous oceans environment. To our knowledge, this paper is the first instantiation of numerical simulation support for control problems of the form (33), (42). We again consider a near control region W_1 and far-field directions $\hat{\mathbf{x}}_1 = (1, \theta_1, \frac{h}{2})$ and $\hat{\mathbf{x}}_2 = (1, \theta_2, \frac{h}{2})$. The control problem is to find the density on the fictitious source $w \in C(\partial D'_a)$ such that for a prescribed field $f_1 \in L^2(\partial W_1)$ and prescribed far-field patterns $f_\infty(\hat{\mathbf{x}}_j) \in \mathbb{C}, \quad j = 1, 2$ the following hold:

$$\begin{cases} u \approx f_1 \text{ in } W_1 \\ u_\infty(\hat{\mathbf{x}}_j) \approx f_\infty(\hat{\mathbf{x}}_j) \end{cases}. \tag{57}$$

where u and u_∞ are defined at (35) and respectively (41). In the last simulation, we will add another control W_2 where we will prescribe a null field. In all simulations, we consider $h = -20$ m, $k = 10$, $n = 100$ and $m = 100$. The unknown density w is expressed in terms of 234 local basis functions. The fictitious source is a sphere of radius 0.01 m centered at
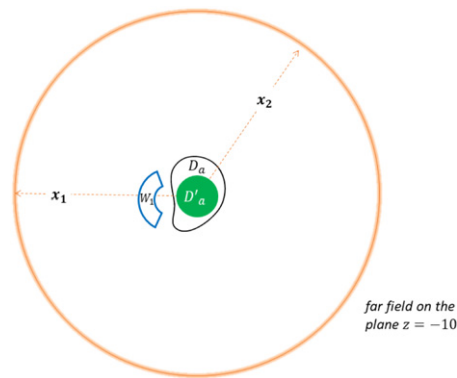
Figure 9. A cross section of the simulation geometry.

(a) Using the default color scheme

(b) Using a truncated color scheme highlighting the reflections from the boundaries
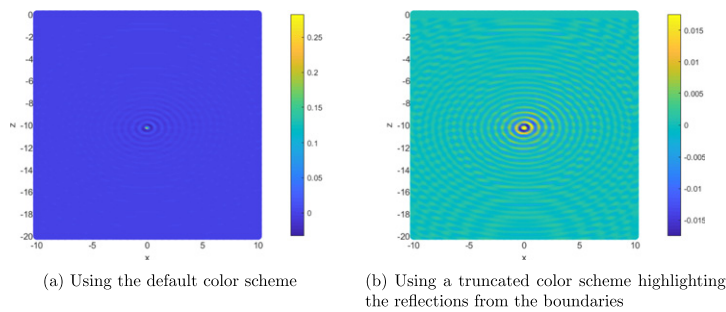
Figure 10. Real part of the generated field on the vertical cross section $y = 0$.

$(0, 0, -10)$ while the actual source is the sphere of radius 0.015 m with the same center. The near control is the annular sector

$$W_1 = \left\{ (r, \theta, \phi) : r \in [0.02, 0.03], \theta \in \left[\frac{\pi}{4}, \frac{3\pi}{4} \right], \phi \in \left[\frac{3\pi}{4}, \frac{5\pi}{4} \right] \right\},$$

and for the last simulation, we have the null control region

$$W_2 = \left\{ (r, \theta, \phi) : r \in [0.15, 0.2], \theta \in \left[\frac{\pi}{4}, \frac{3\pi}{4} \right], \phi \in \left[-\frac{\pi}{4}, \frac{\pi}{4} \right] \right\},$$

both discretized into 4640 collocation points. For simplicity of notations, W_1 and W_2 were given in spherical coordinates (r, θ, ϕ), where r is the radius, $\theta \in [0, \pi]$ is the inclination angle and $\phi \in [0, 2\pi)$ is the azimuthal angle. On the other hand, for consistency with the theoretical framework from the previous section, the far-field directions will be given in cylindrical coordinates (r, θ, z). In the simulations to follow, the far-field directions are $\hat{\mathbf{x}}_1 = (1, \pi, -10)$ directly behind the near control and $\hat{\mathbf{x}}_2 = \left(1, \frac{\pi}{4}, -10 \right)$. A cross section along the middle plane $z = \frac{h}{2}$ of the simulation geometry is shown in figure 9.

As before, we present plots of the prescribed and generated fields on the control region/s for a visual comparison of field pattern. The fields were plotted in a mesh of points slightly off the original mesh used for the collocation scheme as a numerical stability test. Whenever
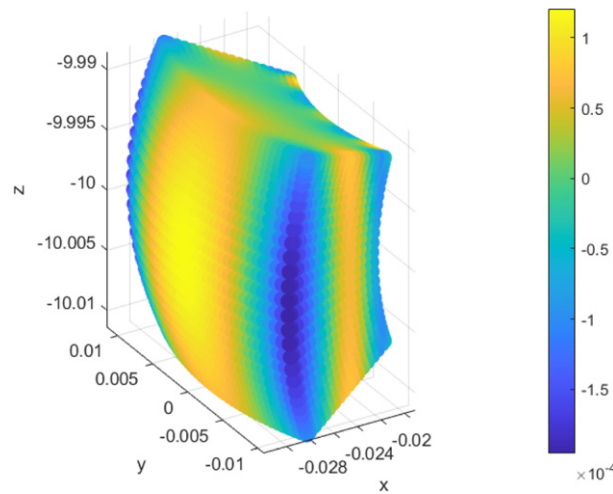
Figure 11. Real part of the generated near field.

applicable, we also plot the pointwise relative errors. The computed normal velocity on the actual source will be characterized by 2D plots of its magnitude, real and imaginary parts in a $\theta\phi$-mesh. We will further describe this surface input by calculating the actual source's average radiated power as defined in (28).

4.2.1. A null near field. In this test, we prescribe a null field on W_1 and the far-field pattern values 0.01 at $\hat{\mathbf{x}}_1$ and 0 at $\hat{\mathbf{x}}_2$. This is a simulation of obstacle-avoiding communication while projecting a quiet zone in a far-field direction. The real part of the generated field on the vertical cross section $y = 0$ is shown in figure 10. The left plot shows the field using the default color bar capturing the entire range of field values. The radiating character of the field is noticeable albeit the very low field values. The plot on the right uses a truncated color bar to reveal the reflections due to the top and bottom ocean boundaries.

The generated near field in the control region W_1 is shown in figure 11. It can be observed that indeed a low signature was generated in W_1 as the field values' magnitude do not exceed 1.96×10^{-4}.

The generated far-field pattern values on some patches around the two fixed directions are shown in figure 12. Around $\hat{\mathbf{x}}_1$, the relative errors reach as high as 2.54%. At $\hat{\mathbf{x}}_1$ the generated value is about $0.0102 - 2.96 \times 10^{-5}$ i with relative error of just 1.78%. Around $\hat{\mathbf{x}}_2$, the values has order 10^{-4}. At $\hat{\mathbf{x}}_2$, the generated value is about $-1.44 \times 10^{-5} + 7.01 \times 10^{-6}$.

The average radiated power of the source is around 1.8071×10^{-5} or about 72.57 dB. Figure 13 shows the corresponding normal velocity on the actual source. It can be observed that the maximum magnitude is just about 6.60×10^{-4}.

4.2.2. A planewave in the near field. In this experiment, we prescribe the plane wave $f(\mathbf{x}) = e^{i\mathbf{x}\cdot(10\mathbf{d})}$ with $\mathbf{d} = [-1, 0, 0]$ on the near control. In the direction of $\hat{\mathbf{x}}_1$ we set a zero far-field pattern value while in $\hat{\mathbf{x}}_2$ we prescribe a value of 0.05. This mimics near-field communication with minimal spill-over behind the near control while projecting a different far-field signature in another direction.

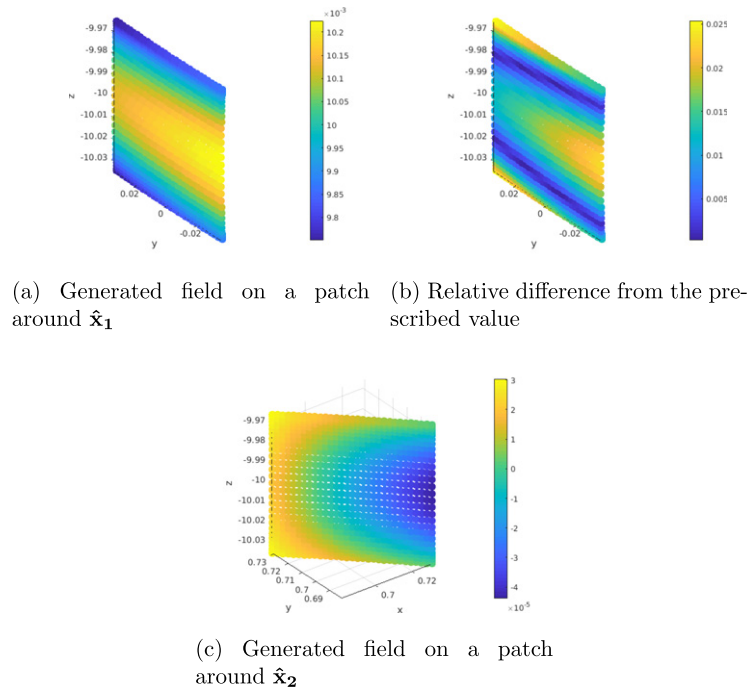Figure 14 shows that the near field is approximated well with a pointwise relative error of at most 2.05%.

(a) Generated field on a patch around $\hat{\mathbf{x}}_1$

(b) Relative difference from the pre-scribed value

(c) Generated field on a patch around $\hat{\mathbf{x}}_2$

Figure 12. Results of the far-field pattern directional control.
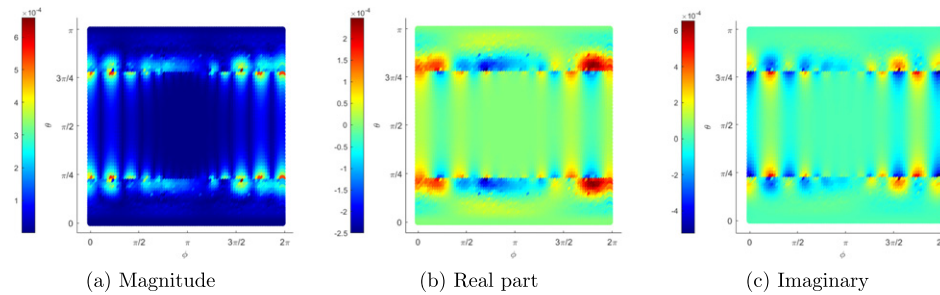

(a) Magnitude

(b) Real part

(c) Imaginary

Figure 13. The computed normal velocity on the actual source.

Figure 15 shows the generated values on the patches around the directions $\hat{\mathbf{x}}_1$ and $\hat{\mathbf{x}}_2$. The values on the patch around $\hat{\mathbf{x}}_1$ are within order 10^{-4}. In the exact direction $\hat{\mathbf{x}}_1$, the generated value has real part $-1.38 \times 10^{-4} + 3.15 \times 10^{-5}$ i. Also, it can be noted that the relative errors on the patch around $\hat{\mathbf{x}}_2$ reach as high as 11%. However, for points very near the exact direction $\hat{\mathbf{x}}_2$, the approximation becomes better. In fact at the exact direction, the generated value is $0.0503 - 1.2 \times 10^{-4}$ i with a relative error of just about 0.60%.

The normal velocity on the physical source for this simulation is shown in figure 16. The average radiated power by the source is around 9.97×10^{-2} or about 109.99 dB.

4.2.3. Two near controls and two far-field directions. In this simulation, we consider an additional near control. Now, we have two near controls (given in spherical coordinates with respect
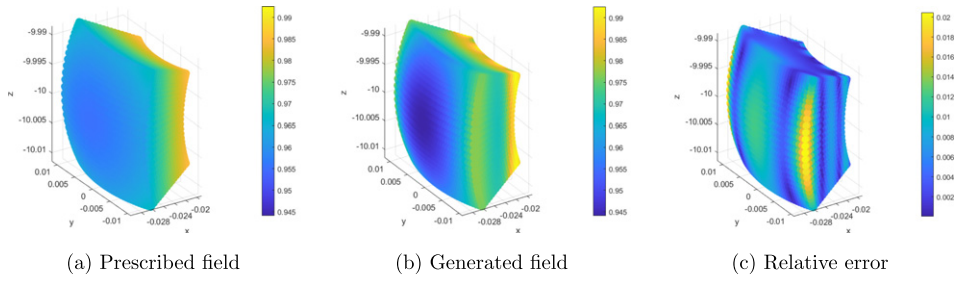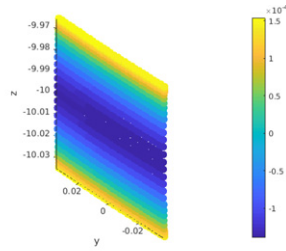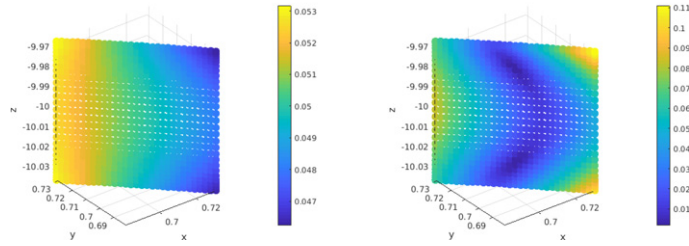
(a) Prescribed field   (b) Generated field   (c) Relative error

Figure 14. Results of the field synthesis on the near control.

(a) Generated field on a patch around $\hat{\mathbf{x}}_1$

(b) Generated field on a patch around $\hat{\mathbf{x}}_2$

(c) Relative difference from the pre-scribed value

Figure 15. Results of the far-field pattern directional control.

to the source's center and where θ is the inclination while ϕ is the azimuthal angle)

$$W_1 = \left\{ (r, \theta, \phi) : r \in [0.02, 0.03], \theta \in \left[\frac{\pi}{4}, \frac{3\pi}{4}\right], \phi \in \left[\frac{3\pi}{4}, \frac{5\pi}{4}\right] \right\}$$

and

$$W_2 = \left\{ (r, \phi, \theta) : r \in [0.15, 0.2], \theta \in \left[\frac{\pi}{4}, \frac{3\pi}{4}\right], \phi \in \left[-\frac{\pi}{4}, \frac{\pi}{4}\right] \right\}.$$

The far-field directions are still given by $\hat{\mathbf{x}}_1 = (1, \pi, -10)$ and $\hat{\mathbf{x}}_2 = \left(1, \frac{\pi}{4}, -10\right)$ in cylindrical coordinates. A cross section of this problem geometry is shown in figure 17.
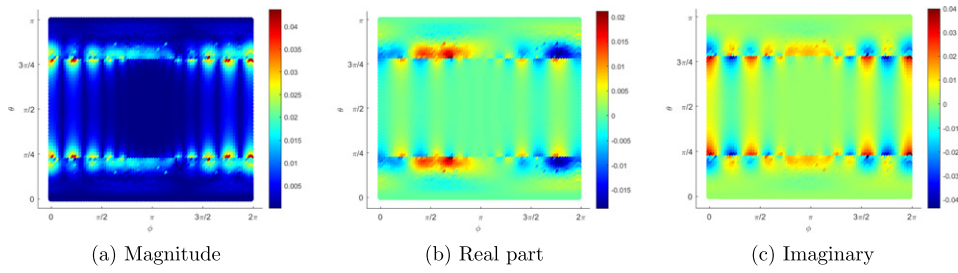
(a) Magnitude   (b) Real part   (c) Imaginary

Figure 16. The computed normal velocity on the actual source.
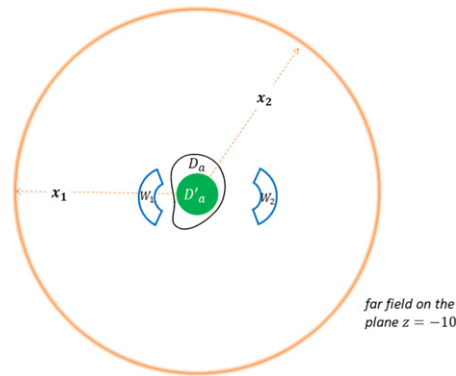
Figure 17. A cross section of the simulation geometry.

(a) Prescribed field   (b) Generated field   (c) Relative error
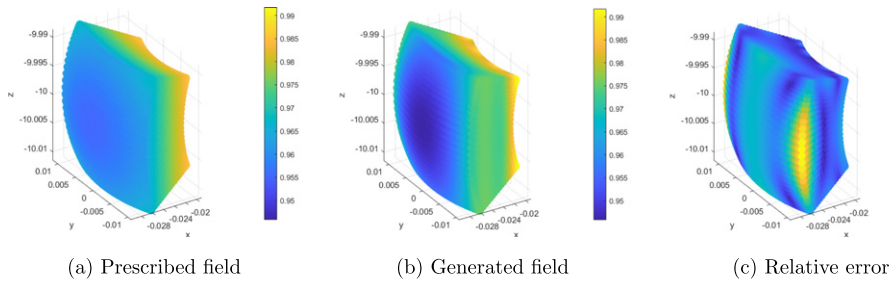
Figure 18. Results of the field synthesis on W_1.

For this simulation we prescribe the outgoing planewave $f(\mathbf{x}) = e^{i\mathbf{x}\cdot(10\mathbf{d})}$ with $\mathbf{d} = [-1, 0, 0]$ on W_1 and a null field on W_2. Then at the direction $\hat{\mathbf{x}}_1$, we prescribe a zero far-field pattern value and at $\hat{\mathbf{x}}_2$ we try to generate 0.05. This test simulates near-field communication on W_1 with minimal spill-over in the direction behind it while keeping W_2 a quiet zone and projecting a decoy pattern in the far-field direction $\hat{\mathbf{x}}_2$.

The results on W_1 are shown in figure 18. The first two plots show a visual comparison between the real parts of the prescribed and generated fields. The third plot shows the pointwise relative error. It can be observed that the relative errors are less than 2.33% all throughout W_1.
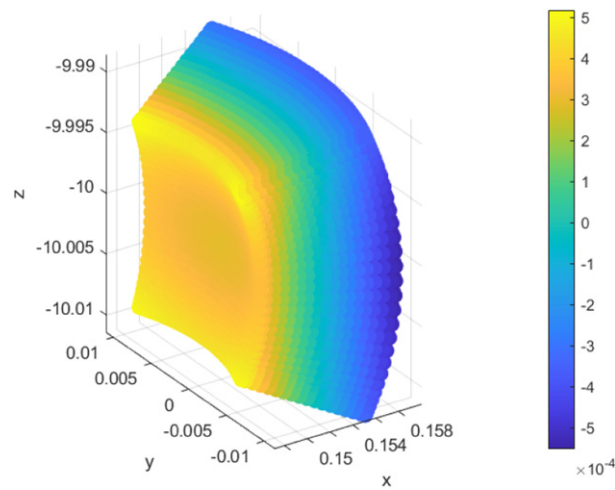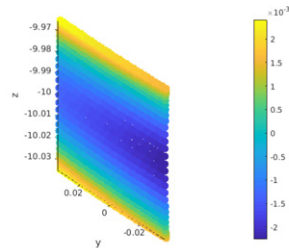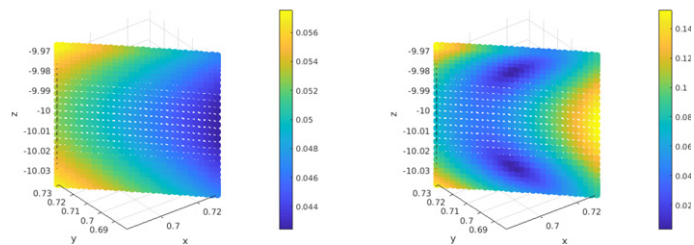
Figure 19. Real part of the generated near field on W_2.

(a) Generated field on a patch around $\hat{\mathbf{x}}_\mathbf{1}$

(b) Generated field on a patch around $\hat{\mathbf{x}}_\mathbf{2}$

(c) Relative difference from the pre-scribed value

Figure 20. Results of the far-field pattern directional control.

Good results were likewise obtained for W_2. Figure 19 shows that the generated field on the second near control is of order 10^{-4}.

In figure 20, the generated far-field pattern values on small patches around the directions $\hat{\mathbf{x}}_1$ and $\hat{\mathbf{x}}_2$ are shown. The values around $\hat{\mathbf{x}}_1$ are all of order 10^{-3}. At the exact direction, the

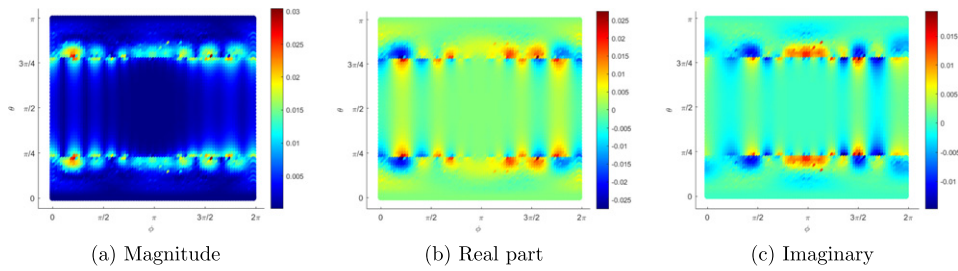(a) Magnitude   (b) Real part   (c) Imaginary

Figure 21. The computed normal velocity on the actual source.

generated value is an order smaller at $4.3 \times 10^{-4} - 1.28 \times 10^{-4}$ i. The decoy pattern is matched well in a smaller subset of the patch around $\hat{\mathbf{x}}_2$. Nevertheless, in the exact direction, the generated value is $0.050\,61 - 1.2 \times 10^{-4}$ i with relative error of only 1.22%.

The computed normal velocity on the actual source is described in figure 21. The average power radiated by the source is about 3.62×10^{-2} or roughly 105.58 dB, a bit lower than the one obtained in the previous simulation.

5. Conclusion and future works

In this paper, we extended the theoretical results and the numerical schemes developed in our previous works on the active control of acoustic fields. We proved the possibility of controlling the acoustic field in the near field of an active source while doing a far-field pattern control in multiple directions in both the free space and a homogeneous finite-depth ocean environment. This was done by showing that for any set of prescribed fields in multiple bounded control regions in the near field and prescribed far-field patterns in distinct directions, one can always find a boundary input on the source, for instance the acoustic pressure on the surface of the source, that will approximate these prescribed fields.

Several numerical simulations in both environments were presented to illustrate the feasibility of the proposed framework. These simulations mimic scenarios in the development of enhanced communication strategies with focus on signal protection and interference avoidance. The results show a good approximation of the desired effects. In all these tests, the source seems to radiate a low average acoustic power.

Our current numerical tests suggest that the solution is stable with respect to various geometric parameters as long as these parameters are within certain problem dependent ranges. In a forthcoming article, we shall provide a sensitivity analysis of our scheme with respect to variations in the frequency and changes in the problem geometry such as the size of the control regions, their distances from the source as well as the number of far-field directions and regions of control and their relative positions. Another future research direction is the use of an array of coupling sources (with fixed or optimized locations) instead of one single source to mitigate possible high amplitudes needed on the boundary input on a single source. The authors are also working on the extension of the results presented for the homogeneous ocean environment to a multi-layered ocean environment. A feasibility study on the possibility of physically instantiating the boundary inputs computed using the strategy proposed here is also forthcoming. These research directions may be aligned with interesting applications such as enhanced communications in free space and underwater environments.

Acknowledgments

ORCID iDs

Neil Jerome A Egarguin ⓘ https://orcid.org/0000-0003-4902-6431

References

[1] Breen S 1995 Uniform upper and lower bounds on the zeros of bessel functions of the first kind *J. Math. Anal. Appl.* **196** 1–17

[2] Buchanan J L, Gilbert R P, Wirgin A and Xu Y S 2004 *Marine Acoustics: Direct and Inverse Problems* (Philadelphia, PA: SIAM)

[3] Buck J R, Preisig J C, Johnson M and Catipovic J 1997 Single-mode excitation in the shallow-water acoustic channel using feedback control *IEEE J. Ocean. Eng.* **22** 281–91

[4] Cheer J 2016 Active control of scattered acoustic fields: cancellation, reproduction and cloaking *J. Acoust. Soc. Am.* **140** 1502–12

[5] Chen S, Lin C and Lu C 2012 Implementation of a feedback active noise control system in a headset *Int. J. Adv. Comput. Technol.* **4** 187–96

[6] Chitre M, Shahabudeen S and Stojanovic M 2008 Underwater acoustic communications and networking: recent advances and future challenges *Mar. Technol. Soc. J.* **42** 103–16

[7] Colton D, Coyle J and Monk P 2000 Recent developments in inverse acoustic scattering theory *SIAM Rev.* **42** 369–414

[8] Colton D and Kress R 2013 *Integral Equation Methods in Scattering Theory* (SIAM Series: Classics in Applied Mathematics   vol 72) (Philadelphia, PA: Society for Industrial and Applied Mathematics)

[9] Colton D and Kress R 2013 *Inverse Acoustic and Electromagnetic Scattering Theory* 3rd edn (Berlin: Springer)

[10] Doicu A, Eremin Y and Wriedt T 2000 *Acoustic and Electromagnetic Scattering Analysis Using Discrete Sources* (New York: Academic)

[11] Egarguin N J A, Onofrei D and Platt E 2020 Sensitivity analysis for the active manipulation of helmholtz fields in 3d *Inverse Problems Sci. Eng.* **28** 314–39

[12] Egarguin N J A, Zeng S, Onofrei D and Chen J 2020 Active control of helmholtz fields in 3d using an array of sources *Wave Motion* **94** 102523

[13] Eggler D, Chung H, Montiel F, Pan J and Kessissoglou N 2019 Active noise cloaking of 2d cylindrical shells *Wave Motion* **87** 106–12

[14] Eggler D and Kessissoglou N 2019 Active acoustic illusions for stealth and subterfuge *Sci. Rep.* **9** 13596

[15] Emerson J F, Chang D B, McNaughton S, Jeong J S, Shung K K and Cerwin S A 2013 Electromagnetic acoustic imaging *IEEE Trans. Ultrason. Ferroelectr. Freq. Control* **60** 364–72

[16] Fadden C and Kothapalli S-R 2018 A single simulation platform for hybrid photoacoustic and rf-acoustic computed tomography *Appl. Sci.* **8** 1568

[17] Han Z, Wu M, Zhu Q and Yang J 2018 Two-dimensional multizone sound field reproduction using a wave-domain method *J. Acoust. Soc. Am.* **144** 1–6

[18] Han Z, Wu M, Zhu Q and Yang J 2019 Three-dimensional wave-domain acoustic contrast control using a circular loudspeaker array *J. Acoust. Soc. Am.* **145** 1–6

[19] Hervella-Nieto L, López-Pérez P M and Prieto A 2019 Robustness and dispersion analysis of the partition of unity finite element method applied to the helmholtz equation *Comput. Math. Appl.* **79** 2426–46

[20] House C, Cheer J and Daley S 2019 An investigation into the performance limitations of active acoustic cloaking using anacoustic quiet-zone *Proc. Acoustics, 178th Meeting of the Acoustical Society of America* (San Diego 2–6 December) p 39

[21] Hubenthal M and Onofrei D 2016 Sensitivity analysis for active control of the helmholtz equation *Appl. Numer. Math.* **106** 1–23

[22] Jensen F B, Kuperman W A, Porter M B and Schmidt H 2011 *Computational Ocean Acoustics* (Berlin: Springer)

[23] Kajikawa Y 2014 Integration of active noise control and other acoustic signal processing techniques *2014 IEEE Asia Pacific Conf. on Circuits and Systems* (APCCAS) pp 451–4

[24] Kajikawa Y, Gan W-S and Kuo S M 2012 Recent advances on active noise control: open issues and innovative applications *APSIPA Trans. Signal Inf. Process.* **1** 1–21

[25] Keller J B and Papadakis J S 1977 *Wave Propagation and Underwater Acoustics* (Lecture Notes in Physics vol 70) (Berlin: Springer)

[26] Kim S-M, Pereira J A, Turra A E and Cho J-H 2017 Modeling and dynamic analysis of an electrical helmholtz resonator for active control of resonant noise *J. Vib. Acoust.* **139** 1–9

[27] Kirby R 2008 Modeling sound propagation in acoustic waveguides using a hybrid numerical method *J. Acoust. Soc. Am.* **124** 1930–40

[28] Kuperman W A and Lynch J F 2004 Shallow-water acoustics *Phys. Today* **57** 55–61

[29] Laureti S, Hutchins D A, Davis L, Leigh S and Ricci M 2016 High-resolution acoustic imaging at low frequencies using 3d-printed metamaterials *AIP Adv.* **6** 121701

[30] Lemoult F, Fink M and Lerosey G 2011 Acoustic resonators for far-field control of sound on a subwavelength scale *Phys. Rev. Lett.* **107** 064301

[31] Lerosey G, Rosny J, Tourin A and Fink M 2007 Focusing beyond the diffraction limit with far-field time reversal *Science* **315** 1120–2

[32] Lin Y-W and Too G-P J 2014 A parametric study of sound focusing in shallow water by using acoustic contrast control *J. Comput. Acoust.* **22** 1450012

[33] Ma C, Kim S and Fang N 2019 Far-field acoustic subwavelength imaging and edge detection based on spatial filtering and wave vector conversion *Nat. Commun.* **10** 1–10

[34] Mahesh K and Mini R S 2019 Helmholtz resonator based metamaterials for sound manipulation *J. Phys.: Conf. Ser.* **1355** 012031

[35] Majid R and Alireza M 2019 Active acoustic cloaking spherical shells *Acta Acust. United Acust.* **104** 5–12

[36] Mao Q, Li S and Liu W 2018 Development of a sweeping helmholtz resonator for noise control *Appl. Acoust.* **141** 348–54

[37] Menzies D 2012 Sound field synthesis with distributed modal constraints *Acta Acust. Acust.* **98** 15–27

[38] Omoto A, Ise S, Ikeda Y, Ueno K, Enomoto S and Kobayashi M 2015 Sound field reproduction and sharing system based on the boundary surface control principle *Acoust. Sci. Technol.* **36** 1–11

[39] Onofrei D 2014 Active manipulation of fields modeled by the helmholtz equation *J. Integr. Equ. Appl.* **26** 553–79

[40] Onofrei D and Platt E 2018 On the synthesis of acoustic sources with controllable near fields *Wave Motion* **77** 12–27

[41] Onofrei D, Platt E and Egarguin N J A 2020 Active manipulation of exterior electromagnetic fields by using surface sources *Q. Appl. Math* (accepted) (https://doi.org/10.1090/qam/1567)

[42] Pan J, Snyder S D, Hansen C H and Fuller C R 1992 Active control of far-field sound radiated by a rectangular panel—a general analysis *J. Acoust. Soc. Am.* **91** 2056–66

[43] Peng D, Gao T and Zeng J 2014 Study on single-mode excitation in time-variant shallow water environment *J. Comput. Acoust.* **22** 1440001

[44] Polycarpou A C 2006 *Introduction to the Finite Element Method in Electromagnetics* (Synthesis Lectures on Computational Electromagnetics) (San Rafael, CA: Morgan & Claypool Publishers)

[45] Poudel J, Lou Y and Anastasio M A 2019 A survey of computational frameworks for solving the acoustic inverse problem in three-dimensional photoacoustic computed tomography *Phys. Med. Biol.* **64** 14TR01

[46] Proakis J G, Sozer E M, Rice J A and Stojanovic M 2001 Shallow water acoustic networks *IEEE Commun. Mag.* **39** 114–9

[47] Simón G M F, Dylan M and Maria F F 2019 Dynamic audio reproduction with linear loudspeaker arrays *J. Audio Eng. Soc.* **67** 190–200

[48] Thompson L L 2006 A review of finite-element methods for time-harmonic acoustics *J. Acoust. Soc. Am.* **119** 1315–30

[49] Zangeneh-Nejad F and Fleury R 2019 Active times for acoustic metamaterials *Rev. Phys.* **4** 100031

[50] Zhang J, Zhang W, Abhayapala T D, Xie J and Zhang L 2019 2.5d multizone reproduction with active control of scattered sound fields *IEEE Explore, ICASSP 2019—2019 IEEE Int. Conf. on Acoustics, Speech and Signal Processing* (*ICASSP*) (May 12–17) pp 141–5

[51] Zhang W, Abhayapala T D, Betlehem T and Maria F F 2016 Analysis and control of multi-zone sound field reproduction using modal-domain approach *J. Acoust. Soc. Am.* **140** 2134–44

[52] Zora M, Buscaino G, Buscaino C, D'Anca F and Mazzola S 2011 Acoustic signals monitoring in shallow marine waters: technological progress for scientific data acquisition *Procedia Earth and Planetary Science: The 2nd Int. Workshop on Research in Shallow Marine and Fresh Water Systems* vol 4 pp 80–92

[53] Zou C and Harne R L 2017 Adaptive acoustic energy delivery to near and far fields using foldable, tessellated star transducers *Smart Mater. Struct.* **26** 055021